In situ grazing-incidence x-ray scattering study of pulsed-laser deposition of Pt layers

V. Holý,[1,2] S. Bauer,[3] A. Rodrigues,[3] L. Horák,[1] X. Jin,[4] R. Schneider,[4] and T. Baumbach[3]
[1]*Department of Condensed Matter Physics, Charles University, Ke Karlovu 5, 121 16 Prague 2, Czech Republic*
[2]*CEITEC, Masaryk University, Kotlářská 2, 611 37 Brno, Czech Republic*
[3]*Institute for Photon Science and Synchrotron Radiation, Karlsruhe Institute of Technology, Hermann-von-Helmholtz-Platz 1, D-76344 Eggenstein-Leopoldshafen, Germany*
[4]*Laboratory for Electron Microscopy, Karlsruhe Institute of Technology, Engesserstr. 7, D-76131 Karlsruhe, Germany*

(Received 30 July 2020; revised 7 September 2020; accepted 11 September 2020; published 28 September 2020)

We present a methodical study of grazing-incidence small-angle x-ray scattering performed *in situ* during pulsed-laser deposition of Pt on sapphire substrates. From measured two-dimensional intensity distributions in reciprocal space we calculated horizontal and vertical intensity projections and compare them to numerical simulations. The structure of the Pt layers was described using a simple Monte-Carlo model and the Ornstein-Zernicke theory with the Percus-Yevick approximation, and the scattering process was simulated using distorted-wave Born approximation. The validity of the structure models as well as the effect of the indirect scattering processes are discussed. From the comparison of the measured and simulated data we determined the lateral and vertical sizes of surface islands, the surface coverage, the island coalescence, as well as the thickness of the wetting layer at the substrate surface. We studied the time evolution of these parameters and their dependence on the substrate temperature.

DOI: 10.1103/PhysRevB.102.125435

I. INTRODUCTION

Grazing-incidence small-angle x-ray scattering (GISAXS) has been frequently used for *in situ* investigation of thin film growth realized by various deposition techniques; see the reviews [1–3], among others. Measured reciprocal-space distribution of diffusely scattered intensity $I(\boldsymbol{Q})$ is used for the determination of the *lateral* size of characteristic surface features (islands, ripples, terraces, etc.) as well as for the study of *vertical* structure (layer thicknesses, island heights, etc.); here we denote $\boldsymbol{Q} = \boldsymbol{K}_\mathrm{f} - \boldsymbol{K}_\mathrm{i}$ the scattering vector, $\boldsymbol{K}_{\mathrm{i,f}}$ being the wave vectors of the primary and scattered beams.

The lateral surface structure is usually manifested by characteristic side maxima of $I(\boldsymbol{Q})$; in many papers the lateral position $\boldsymbol{Q}_{\parallel\mathrm{m}}$ of the maxima is used for a simple estimation of the lateral size of the surface features by fitting the maxima to a suitable phenomenological peak function [4–11]. In Refs. [9,10,12–17] *in situ* recorded GISAXS data were compared to numerical simulations based on the paracrystal model [18,19]. The paracrystal model is implemented in standard software packages available for GISAXS simulations and fitting [20,21]. The fitting to the paracrystal model can determine the mean lateral island size and its statistical distribution, as well as mean island-island distances. However, the paracrystal model is purely phenomenological and it does not correctly consider physical processes during the deposition. Moreover, the resulting parameters can be affected by *a priori* assumptions on statistical correlation between the island sizes and distances, especially in the case of densely packed islands (see the discussion in Ref. [1]). For the description of the correlation function of densely packed objects the Ornstein-Zernicke (OZ) theory [22] is more appropriate, albeit it is still rather phenomenological. This method takes into account many-particle interactions and it is mainly used in the theory of fluids. The OZ model can be solved under assumption of nonpenetrating rigid particles using the Percus-Yevick (PY) model [23]. For the analysis of GISAXS data this approach is seldom used and to our knowledge it has not been applied so far for *in situ* data.

Numerical Monte-Carlo (MC) methods take into account atomistic processes on the growing surface and they use true physical parameters of growth (temperature, diffusivities, diffusion barriers, interaction energies, etc.); see the reviews in Refs. [24–27]. In contrast to the previously mentioned approaches, these methods correctly describe the island ripening, coalescence, and percolation. On the other hand, the numerical realization of a MC method is rather time consuming and it can be hardly used for fitting of large datasets.

For the description of the vertical sample structure, x-ray scattering from the substrate and from a thin wetting layer at the substrate surface (if present) must be correctly included. Usually, distorted-wave Born approximation (DWBA) is used, in which not only the primary wave but also the waves specularly reflected from and transmitted through the flat interfaces are diffusely scattered from the islands [28].

In this paper we compare the PY model with simple Monte-Carlo simulations and study the growth and coalescence of surface islands. From the comparison we identify structure parameters which can be determined using both approaches. Using DWBA we determine also the time evolution of the island heights and the wetting-layer thickness. The method is used for the analysis of *in situ* GISAXS data acquired during

pulsed-laser deposition (PLD) of thin Pt layers on sapphire substrates, and we demonstrate that the growth kinetics is substantially affected by the substrate temperature. This work presents a methodical study, a detailed extensive investigation of a large set of growth conditions will be the subject of a forthcoming paper.

II. EXPERIMENTS

Here we report two growth runs of Pt layers by pulsed-laser deposition (PLD) at two different temperatures $T = 300\,^{\circ}\mathrm{C}$ (growth run I) and $T = 500\,^{\circ}\mathrm{C}$ (growth run II) for a duration of one hour. The Pt layers were deposited using the same fluence of 40 J/cm^2, the repetition frequency of 5Hz, and laser spot size on the target of 0.05×0.03 cm^2. The target-substrate distance utilized for the PLD growth was 35 mm. *In situ* GISAXS measurements were performed during noninterrupted PLD growth runs I and II with the acquisition time of 10 s at NANO beamline of the Institute of Photon Science and Synchrotron Radiation (IPS) at the KARA storage ring of Karlsruhe, Germany. The x-ray beam had an energy of 15 keV and a beam size in FWHM of 250 μm (horizontal) $\times$ 80 μm (vertical); the angle of incidence was set to 0.7 deg. Using a 111Si monochromator, we achieved the energy resolution of about $\Delta E/E \approx 10^{-4}$; horizontal and vertical divergences of the primary beam were 0.05×0.004 mrad^2. These values result in the coherence length and width of about 1 μm and 2 μm, respectively. A two-dimensional (2D) detector (Pilatus 2M, 1475×1679 pixels, pixel size of $172 \times 172\,\mu$m^2) was used at a sample-to-detector distance of 2316 mm. The *in situ* PLD chamber which is used for Pt growth is well suited for *in situ* x-ray diffraction and for *in situ* grazing incidence diffraction and is previously described in detail in Refs. [29,30].

The topography of the Pt layers was characterized by scanning electron microscopy (SEM) using an FEI Dual beam Helios G4 FX microscope. For this purpose, the microscope was operated at 2 kV accelerating voltage in the so-called immersion mode with a beam current of approximately 0.1 nA and the through-lens detector (TLD) was used for secondary electron (SE) imaging of the sample surface. This microscope setup helped to obtain a very good lateral resolution in SE imaging in combination with a high surface sensitivity. In particular, the size of the interaction volume was reduced because of the low primary electron energy of only 2 keV compared to standard values of 10 keV and more. In addition, the sample was tilted by about 20 deg or 40 deg in order to get a more three-dimensional impression of the surface relief.

III. THEORY

We model the growing surface by a large set of cylindrical islands. The island positions $\boldsymbol{x}_j \equiv (x_j, y_j)$, radii R_j, and heights h_j are random and statistically independent, and we assume that the surface is statistically homogeneous, i.e., the mean radii and heights $R = \langle R_j \rangle$, $h = \langle h_j \rangle$ do not depend on the sample positions, and the mean coverage of the surface by the islands θ does not depend on $\boldsymbol{x}$, either ($0 \leqslant \theta \leqslant 1$ holds). In order to include possible coalescence of islands, we consider also penetrating islands.

For the simulation of x-ray scattering we used the distorted-wave Born approximation method (DWBA) [28,31]. In this approach, the sample is divided into two parts, a nondisturbed part with flat interfaces and a disturbance. In our case, the nondisturbed system comprises a semi-infinite sapphire substrate, a Pt wetting layer with thickness T_{Pt}, and an effective "diluted" Pt layer with the thickness h and electron density $\theta\varrho_{\mathrm{Pt}}$, where ϱ_{Pt} is the electron density of bulk Pt. In the DWBA, the set of islands is irradiated by the waves transmitted through the diluted layer (with the wave vector $\boldsymbol{k}_T^{(1)}$ and amplitude $E_T^{(1)}$) and reflected from the Pt wetting layer underneath with the wave vector $\boldsymbol{k}_R^{(1)}$ and the amplitude $E_R^{(1)}$. Similarly, the wave scattered from the islands is transmitted again through the diluted layer; its wave vector and amplitude are $\boldsymbol{k}_T^{(2)}$ and $E_T^{(2)}$ or reflected again from the wetting layer (wave vector $\boldsymbol{k}_R^{(2)}$ and amplitude $E_R^{(2)}$). This approximation assumes that the islands are vertically homogeneous cylinders so that the effective diluted layer is vertically homogeneous, too. Thus, the wave irradiating the cylinders decays vertically only due to absorption in the diluted layer; the absorption is rather weak since the angle of incidence is far above the critical angle of total reflection. Moreover, the extinction of this wave due to scattering from the islands is not considered. The consequence of this simplification is that the scattering from the bottom parts of the islands is slightly overestimated.

The intensity of diffuse scattering is

$$I(\boldsymbol{Q}) = SPC^{(\mathrm{FT})}(\boldsymbol{Q}_\parallel) \sum_{\alpha=1}^{4} \sum_{\beta=1}^{4} \frac{A_\alpha A_\beta^*}{q_\alpha q_\beta^*} \langle (e^{-iq_\alpha h} - 1)(e^{iq_\beta^* h} - 1) \rangle_h . \tag{1}$$

Here S is the irradiated surface area and P is a constant containing the primary intensity and the factor $\delta_{\mathrm{Pt}}(1-\theta)$, i.e., the contrast in the refraction index increment $\delta = 1 - n$ of the islands and diluted layer. We assume that the islands are made of pure Pt with the nominal increment δ_{Pt} and the increment of the diluted layer is $\theta\delta_{\mathrm{Pt}}$.

The sums over α and β run over the scattering processes, A_α and q_α are the amplitudes, and the vertical components of the scattering vectors of the processes, listed in the table in Fig. 1. If we restrict ourselves only to the first ("direct") process $\alpha = \beta = 1$, we neglect diffuse scattering of specularly reflected wave and specular reflection of diffusely scattered wave (kinematical approximation). This simplification can be used if the specular reflectivity is weak, due to large interface roughness and/or large incidence/exit angles, for instance. Figure 1 shows the dependences of individual scattering processes intensities $|A_\alpha|^2$ on the vertical component Q_z of the scattering vector, calculated for the typical values $\theta = 0.5$, $h = 5$ nm, $T_{\mathrm{Pt}} = 1$ nm, and $\alpha_{\mathrm{i}} = 0.7$ deg; the intensities are normalized to the primary intensity, and the sharp peaks at $Q_z \approx 1$ nm^{-1} are the Yoneda wings. From the figure, the effect of the "indirect" scattering processes ($\alpha = 2, 3, 4$) is obvious. The direct process $\alpha = 1$, the indirect process $\alpha = 2$ is not negligible close to the Yoneda wing, the intensity of process $\alpha = 3$ is almost one percent of α_1 for all Q_z's, and the process $\alpha = 4$ can be neglected. The averaging $\langle\,\rangle_h$ in Eq. (1) runs over random island heights h. Further, $\boldsymbol{Q}_\parallel$ is the in-plane component of all scattering vectors, i.e., $\boldsymbol{Q}_\parallel = \boldsymbol{k}_{T,R\parallel}^{(2)} - \boldsymbol{k}_{T,R\parallel}^{(1)}$.

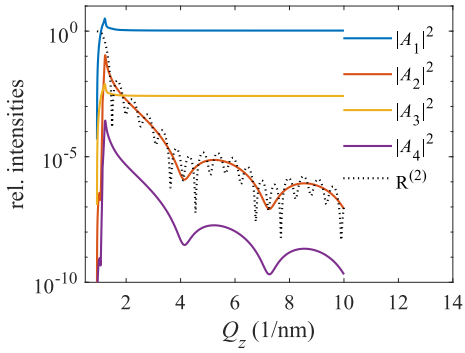

α	A_α	q_α
1	$E_T^{(1)}E_T^{(2)}$	$k_{Tz}^{(2)} - k_{Tz}^{(1)}$
2	$E_T^{(1)}E_R^{(2)}$	$k_{Rz}^{(2)} - k_{Tz}^{(1)}$
3	$E_R^{(1)}E_T^{(2)}$	$k_{Tz}^{(2)} - k_{Rz}^{(1)}$
4	$E_R^{(1)}E_R^{(2)}$	$k_{Rz}^{(2)} - k_{Rz}^{(1)}$

FIG. 1. The intensities of individual scattering processes normalized to the primary intensity as function of Q_z. See the main text for the details. The black dotted line depicts the reflectivity curve calculated for variable exit angles α_f derived from Q_z and α_i, the scattering processes $\alpha = 1, \ldots, 4$ are defined in the table in the right panel.

This component also equals the in-plane component of the vacuum scattering vector $\boldsymbol{Q}$.

Finally,

$$C^{(\mathrm{FT})}(\boldsymbol{Q}_\parallel) = \int d^2\boldsymbol{x}\, C(\boldsymbol{x}) e^{-i\boldsymbol{Q}_\parallel \cdot \boldsymbol{x}} \tag{2}$$

is the Fourier transformation of the correlation function of the surface, which depends both on the island positions and sizes. We define the random function $p(\boldsymbol{x})$, which equals one if the point $\boldsymbol{x} \equiv (x, y)$ at the surface is covered by an island, otherwise it is zero; the mean value of $p(\boldsymbol{x})$ equals the coverage $\langle p(\boldsymbol{x})\rangle = \theta$. The correlation function is then

$$C(\boldsymbol{x}) = \langle p(\boldsymbol{x}) p(0)\rangle - \theta^2. \tag{3}$$

In Eqs. (1)–(3) the averaging runs over all possible island configurations ("microstates"). We assume that the island distribution is statistically homogeneous and isotropic, then the correlation function depends only on the length $\rho \equiv |\boldsymbol{x}|$ and its Fourier transformation can be expressed by the Hankel transform

$$C^{(\mathrm{FT})}(Q_\parallel) = 2\pi \int_0^\infty d\rho\, \rho\, C(\rho) J_0(Q_\parallel \rho), \tag{4}$$

where J_0 is the Bessel function of zeroth order.

The asymptotic behavior of $C(\rho)$ is obvious:

$$\lim_{\rho\to\infty} C(\rho) = 0, \quad \lim_{\rho\to 0} C(\rho) = \theta - \theta^2. \tag{5}$$

The second limit occurs in the integral $S_z(Q_z) = \int_0^\infty dQ_\parallel Q_\parallel I(\boldsymbol{Q})$ calculating the vertical intensity projection (see the next section), unfortunately this fact cannot be simply used for the estimation of θ, since the integral depends also on the vertical sample structure.

From Eq. (1) it follows that the diffusely scattered intensity is assumed as a product of two functions, one depends on $Q_\parallel$ and is affected only by the lateral shapes of the islands, where the other depends on the vertical component Q_z of the scattering vector $\boldsymbol{Q}$; this function depends only on the island heights. This fact follows from the assumed cylindrical shapes of islands and it is used in the analysis of experimental data, in which the lateral and vertical intensity distributions are analyzed separately.

For the calculation of $C(\boldsymbol{x})$ we developed a simple phenomenological Monte-Carlo model which allows us to determine the basic parameters of the growing surface. The model describes the transition from the isolated-island morphology to the coalesced structure. In the model we assume that cylindrical islands are randomly placed in a square

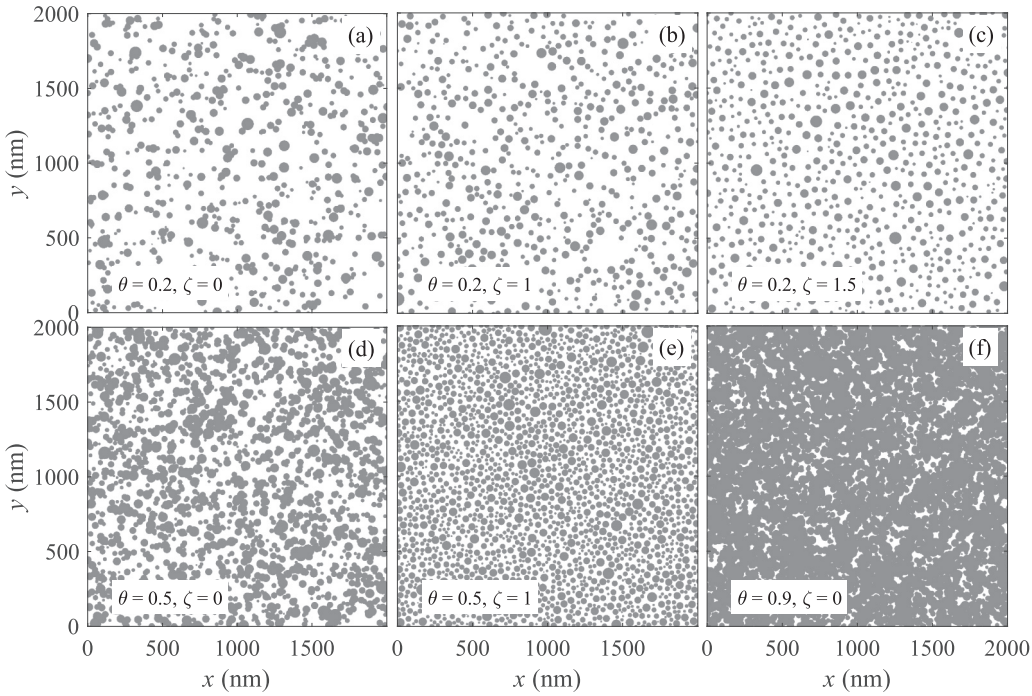

FIG. 2. Distributions of islands simulated for various θ and ζ (parameters of the panels) and the same mean island radius of $R = 20$ nm.

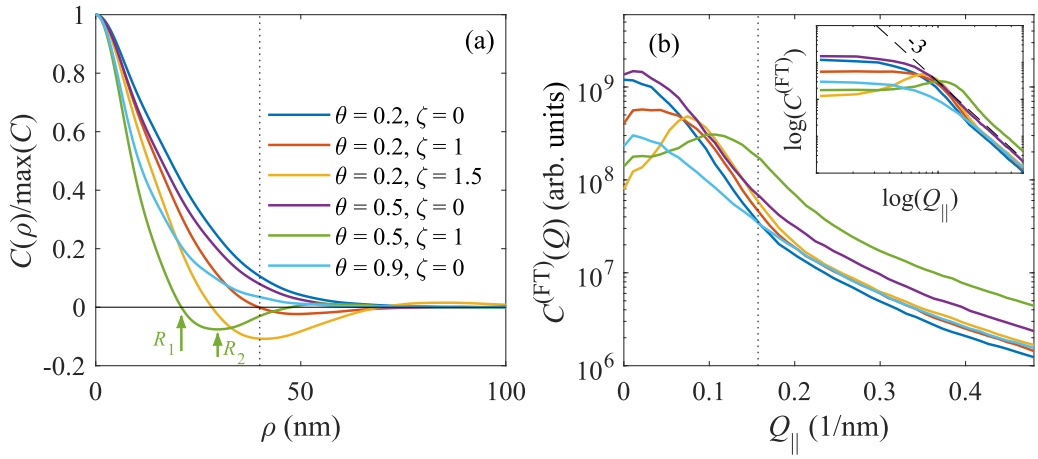

FIG. 3. The correlation functions $C(\rho)$ (a) and their Hankel transformations $C^{(FT)}(Q_\parallel)$ (b) calculated for various values of θ and ζ using our MC method. The vertical dotted lines are at $\rho = 2R$ and $Q_\parallel = \pi/R$ in panels (a) and (b), respectively. The inset in (b) demonstrates that $C^{(FT)}(Q_\parallel)$ asymptotically decays as $Q_\parallel^{-3}$. In panel (a), the characteristic radii $R_{1,2}$ are denoted by vertical arrows.

simulation area with the size $L \times L$, assuming periodic boundary conditions for the calculation of the nearest island distance. The island radii R_j are random and they are distributed according to Gamma distribution with the mean value R and the order m_R; the root-mean square (rms) deviation of the radii is $\sigma_R = R/\sqrt{m_R}$. For the generation of random island positions we assume that there is no island-island interaction, however the distance $d_{jk} = |\boldsymbol{x}_j - \boldsymbol{x}_k|$ of the centers of the islands j and k must be larger than $\zeta(R_j + R_k)$. The parameter $\zeta = R_{D,j}/R_j$ determines the radius $R_{D,j}$ of the depleted zone around the jth island relative to R_j, where no other islands can occur. In the definition of parameter ζ we take into account the actual (random) island radii $R_{j,k}$. If $\zeta = 1$, $R_{D,j} = R_j$ and we allow touching of nonpenetrating islands; the case $\zeta = 0$ describes the island coalescence. The island heights h_j have been assumed random as well and independent from the island radii, we assume the Gamma distribution with the mean height $h = \langle h_j \rangle$ and the order m_h; the rms deviation of the heights is $\sigma_h = h/\sqrt{m_h}$. The MC simulation was performed $N > 10^3$ times with various starting seeds of the random generator; each simulation corresponds to one microstate. The resulting correlation function $C(\rho)$ was obtained by averaging of the set of correlation functions of individual microstates. The surface coverage of the ith microstate is $\theta_i = \sum_j \pi [R_j^{(i)}]^2/L^2$ and the mean coverage $\theta = \sum_i \theta_i/N$. The size L of the simulation area roughly compares to the size of coherently irradiated volume (CIV), determined mainly by the coherence length of the primary beam; therefore, one microstate occurs in one CIV. The averaging over the microstates corresponds to the fact that in an experiment the irradiated footprint contains approx. 10^6 CIVs.

Figure 2 shows examples of the surface morphologies simulated for various θ and ζ; in the figures gray (white) areas denote the island and the gaps between the islands, respectively. In the simulations we set $R = 20$ nm, $m_R = 10$, and $L = 2000$ nm. In Fig. 3 we plot the correlation functions $C(\rho)$ [panel (a)] and their Hankel transformations $C^{(FT)}(Q_\parallel)$ (b) calculated for the same sets of parameters. The Hankel transformation was calculated numerically according to Eq. (4). The upper limit of the numerical integral equals L, which determines the step size of $Q_\parallel$ to approx. 3×10^{-3} nm^{-1}. The figure clearly demonstrates that the correlation function of a noncoalesced island set shows a negative minimum, while that of a coalesced structure has the form of one central maximum and negative side minima are missing. Therefore, the extinction of the negative minimum of the correlation function can be considered as the onset of the island coalescence. Similarly, the function $C^{(FT)}(Q_\parallel)$, which is proportional to the $Q_\parallel$ dependence of the scattered intensity, shows a side maximum in a noncoalesced case. In Fig. 3(a) we define characteristic radii $R_{1,2}$ of the surface; the former is the first zero point of $C(\rho)$, where the latter corresponds to its (negative) minimum. In the next chapter we determine the time evolution of these radii from experimental data. From the figure it is obvious that there is no simple connection between the characteristic radii $R_{1,2}$ and the values R and R_D. For instance, for the typical coverage of $\theta = 0.5$ and touching islands ($\zeta = 1$), R_1 corresponds roughly to R, however R_1 increases with decreasing coverage or increasing

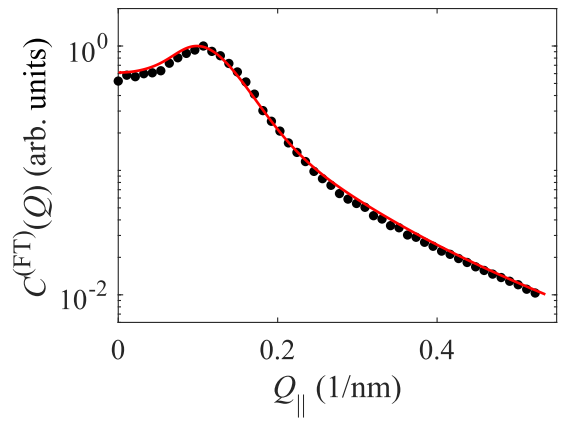

FIG. 4. The correlation function $C^{(FT)}(Q_\parallel)$ calculated for $\theta = 0.5$ and $\zeta = 1$ using our MC method (points) and the Percus-Yevick model [33] (line).

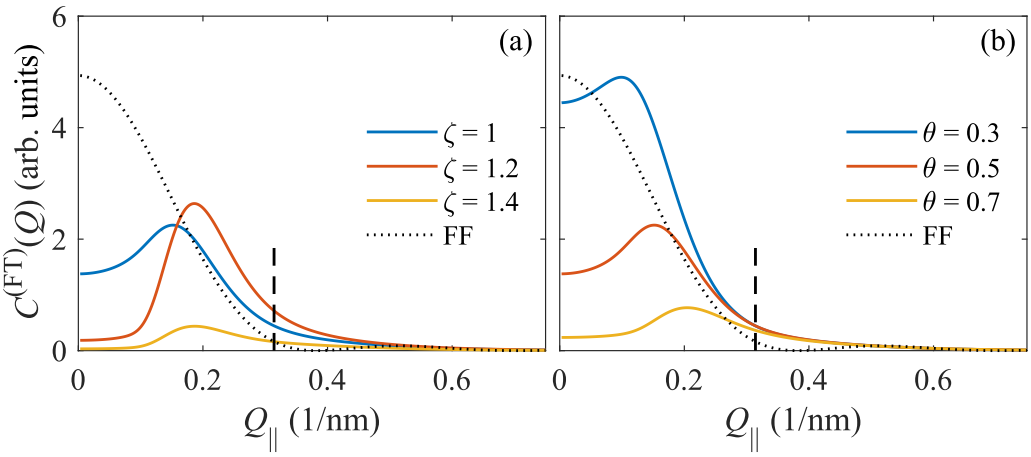

FIG. 5. The correlation function $C^{(FT)}(Q_{\|})$ calculated using the Percus-Yevick model for various ζs and constant $\theta = 0.5$ (a), and for various θs and constant $\zeta = 1$ (b). The mean island radius was set to $R = 10$ nm and $m_R = 10$. The vertical dashed lines denote the value of π/R. The black dotted curves represent only the island form factor (not in scale), which is proportional to the correlation function for $\theta \to 0$.

ζ. The inset of Fig. 3(b) demonstrates that the asymptotic tails of $C^{(FT)}(Q_{\|})$ behave as $Q_{\|}^{-3}$; this fact corresponds to the Porod's scattering from a surface fractal with dimension $D = 3$ [32].

In addition to the MC method, the island distribution with $\zeta \geqslant 1$ can also be described using the Ornstein-Zernicke theory [22] with Percus-Yevick model [23], which was reformulated for nonpenetrating "hard" cylindrical discs in Ref. [33]. Figure 4 compares the correlation functions $C^{(FT)}(Q_{\|})$ using the MC method and the PY model for $\theta = 0.5$, $\zeta = 1$ and $R = 20$ nm, $m_R = 10$. Indeed, both methods yield very similar results. The PY model is much faster, since it uses an explicit formula (see Ref. [33]), however it does not include the island coalescence, so that it cannot be used for the analysis of experimental data at later growth stages. The PY model was implemented also in the well-known FitGISAXS software package [21], which might be used for the fitting as well.

Figure 5 presents a series of calculations of $C^{(FT)}(Q_{\|})$ using the PY model for various values of ζ and θ. It is obvious that the position $Q_{\|m}$ of the side maximum (and consequently the position of the satellite peak in the scattered intensity) is slightly affected both by the coverage θ and by the depletion factor ζ. Therefore, the position $Q_{\|m}$ alone can be used only for the estimate of the radius $R_m = \pi/Q_{\|m}$, which agrees with the mean radius R only with the accuracy of several tens of percent. For a more exact estimate of R and for the determination of θ and ζ the fitting of the whole curve to the PY model must be performed. However, for a coalesced structure the PY model is not applicable, and we can estimate only the characteristic radii $R_{1,2}$ mentioned above.

Now we focus attention to the distribution of the diffusely scattered intensity along the vertical Q_z axis. From Eq. (1) it follows that the vertical distribution is determined mainly by the mean height h of the islands and by the thickness T_{Pt} of the Pt wetting layer. Figure 6 shows the simulated intensities as functions of h and Q_z [panels (a) and (b)] and functions of T_{Pt} and Q_z (c),(d); in the simulations we replaced the lateral correlation function by its value in zero $C(0) = \theta - \theta^2$ and used the values $\theta = 0.5$ and $\sigma_h = 0$.

The Q_z dependence of the diffusely scattered intensity shows maxima ascribed to island thickness fringes, and their positions can be derived considering only process $\alpha = 1$. The scattered intensity is roughly proportional to $|\mathrm{sinc}(q_1 h/2)|^2$, where $q_1 = k_{Tz}^{(2)} - k_{Tz}^{(1)}$ and $\mathrm{sinc}(x) = \sin(x)/x$. The nonzero maxima of this function are in the points $q_{1m} \approx (2m+1)\pi/h$, from which the following simple formula for the maximum positions can be derived

$$Q_{zm} = K\sin(\alpha_i) + K\sqrt{\left[\frac{\pi(2m+1)}{hK} - \sqrt{\sin^2(\alpha_i) - 2\delta_{eff}}\right]^2 + 2\delta_{eff}}. \quad (6)$$

Here we denoted $K = 2\pi/\lambda$, $\alpha_i = 0.7$ deg is the incidence angle, $m = 0, 1, 2, \ldots$, and $\delta_{eff} = \theta \mathrm{Re}(\delta_{Pt})$. This result shows that it is possible to determine the mean height h of the islands from the measured Q_z dependence of the diffusely scattered intensity. The intensity distribution is less sensitive to the Pt wetting layer under the islands. We repeated the simulations for various θ's and we found the same hyperbolic shape of the interference maxima. It is worthy to note that the scattered intensity in panels (c),(d) does not depend on T_{Pt}, if only the direct process $\alpha = 1$ is considered, thus the T_{Pt} dependence reflects the importance of the indirect processes $\alpha = 2, 3, 4$.

Figure 7 displays in detail the region of the Yoneda wing and its dependence on θ. The Yoneda wing occurs for the Q_z value that corresponds to the exit angle of the scattered radiation, which equals the critical angles of total external reflection for sapphire or Pt. In Figs. 6 and 7 the positions of the Pt and sapphire Yoneda wings are denoted by horizontal blue dashed lines. From the figure it follows that for zero or

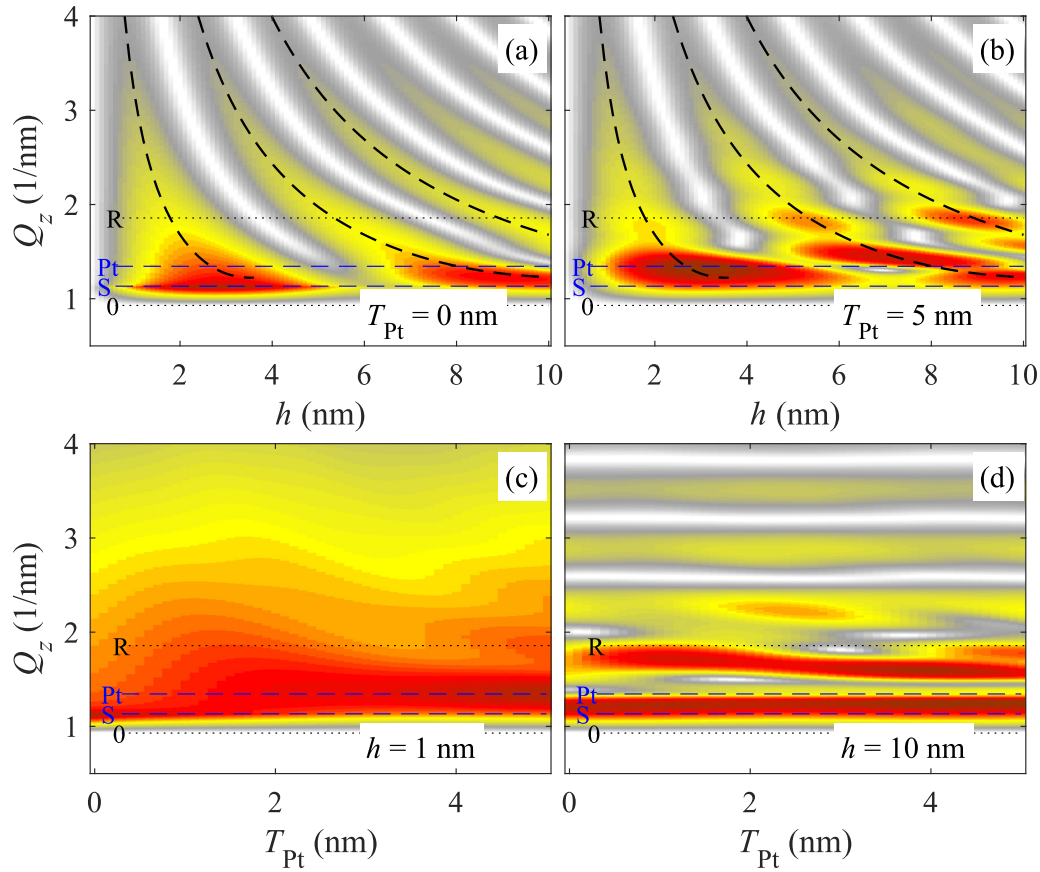

FIG. 6. The distributions of diffusely scattered intensity along the Q_z axis calculated as functions of the mean island height h for two thicknesses T_{Pt} of the wetting layer (a),(b) and as functions of T_{Pt} for two values of h (c),(d). In the calculations we kept the coverage $\theta = 0.5$ fixed. The dotted horizontal lines marked "0" and "R" denote the Q_z values for the zero exit angle (0—the sample horizon) and for the specularly reflected beam (R), the blue dashed lines denote the positions of the Yoneda wings for Pt (upper line) and sapphire (lower line). The dashed hyperbolas in (a),(b) denote the positions of diffuse maxima following from Eq. (6). The colors of the two-dimensional graphs (from white to dark red) span over two decades.

very thin Pt wetting layers, the position of the intensity maximum on the Q_z only very slightly depends on the coverage θ and it coincides with the Yoneda wing of sapphire [panel (a), the black dots] for almost all coverages θ. Only for a thicker wetting layer in Fig. 7(b), the maximum moves towards the Pt Yoneda wing with increasing coverage. Therefore, from the Q_z position of the diffuse intensity maximum it is possible to estimate the coverage θ only qualitatively.

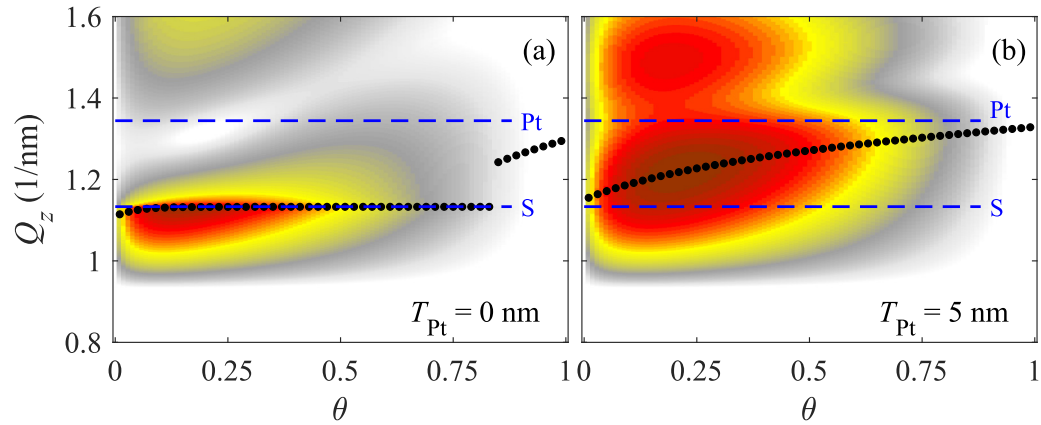

FIG. 7. The diffusely scattered intensities calculated as functions of coverage θ and Q_z in the vicinity of the sapphire and Pt Yoneda wings (blue dashed lines denoted "S" and "Pt," respectively), for fixed island height $h = 5$ nm. The black dots represent the intensity maxima on the Q_z axis. The colors of the two-dimensional graphs (from white to dark red) span over three decades. In panels (a) and (b) we put $T_{Pt} = 0$ and 5 nm, respectively.

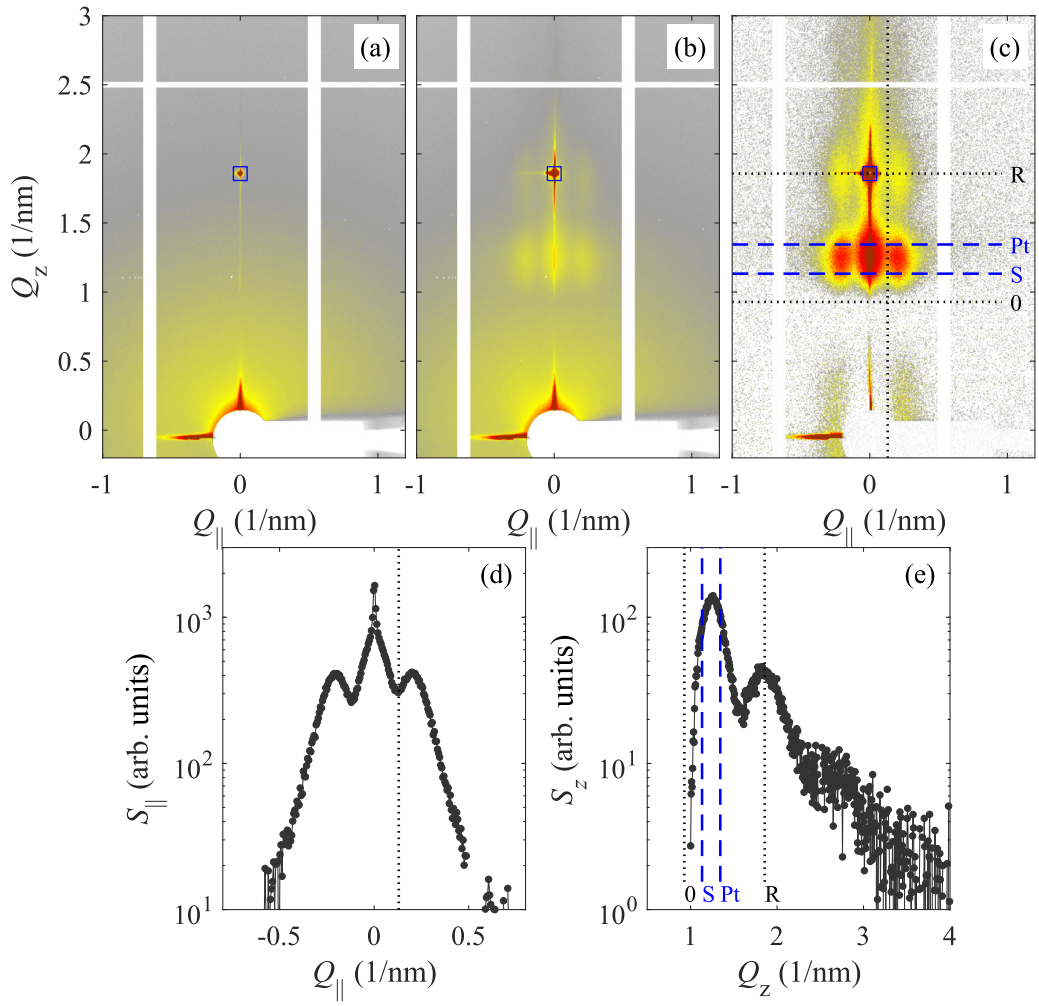

FIG. 8. Examples of the experimental data: (a) The GISAXS pattern of the sapphire substrate before the deposition, growth run I, (b) the GISAXS pattern after 285s deposition, (c) the same pattern after subtraction of (a). Panels (d) and (e) display the horizontal and vertical projections of (c), respectively. In (c), the horizontal black dotted lines denote the values of Q_z corresponding to the sample horizon (0) and of the specularly reflected maximum (R). The blue dashed lines denote the positions of the Yoneda wings for sapphire (S) and Pt. The vertical dotted line denotes the minimum value $Q_{\|\min}$, from which the vertical projection in (e) was calculated. The blue rectangles in (a)–(c) denote the areas from which the specularly reflected intensity was extracted. The color scale in (a)–(c) is logarithmic and the colors from white to dark red span over three decades.

IV. ANALYSIS OF THE GISAXS DATA

During each growth run several thousands of GISAXS patterns have been collected; typical examples of the GISAXS patterns taken before and during the growth run I are shown in Figs. 8(a) and 8(b). From each pattern we subtracted the pattern of the naked sapphire substrate; this removes the air scattering and possible influence of the windows of the growth chamber [panel (c)].

It is not practical to fit the whole 2D reciprocal-space maps of measured intensity to the theory. Instead, we considered horizontal $S_{\|}(Q_{\|}, t)$ and vertical $S_z(Q_z, t)$ projections shown in Figs. 8(d) and 8(e) using the expressions

$$S_{\|}(Q_{\|}) = \int_{Q_z^{(\mathrm{sappire})}}^{Q_z^{(\mathrm{Pt})}} dQ_z I(\boldsymbol{Q}),\ S_z(Q_z) = 2\pi \int_{Q_{\|\min}}^{\infty} dQ_{\|} Q_{\|} I(\boldsymbol{Q}). \tag{7}$$

For the horizontal projections we took into account the GISAXS data with the Q_z coordinates between the positions of the Yoneda wings of sapphire and Pt $Q_z^{(\mathrm{sapphire})} \leqslant Q_z \leqslant Q_z^{(\mathrm{Pt})}$; the $Q_z^{(\mathrm{sapphire,Pt})}$ values are denoted in Fig. 8(c) by horizontal blue dashed lines. For the vertical projection we integrated the GISAXS data along $Q_{\|}$ for $Q_{\|} > Q_{\|\min}$, where $Q_{\|\min}$ [vertical dotted line in panel (c)] was chosen so that the projection does not include the central specular maximum. In the $Q_{\|}$ integration we assumed that the experimental intensity pattern exhibits a circular symmetry in the Q_xQ_y plane, and the $Q_{\|}$ integral is in fact a 2D integral over the area $|\boldsymbol{Q}_{\|}| > Q_{\|\min}$. In contrast to usual practice, which uses vertical *cuts* of the experimental 2D pattern (see Refs. [10,14], for instance), we use *projections* into the Q_z axis. Since

$$2\pi \int_0^{\infty} dQ_{\|} Q_{\|} C(Q_{\|}) = \int d^2\boldsymbol{Q}_{\|} C(\boldsymbol{Q}_{\|}) = 4\pi^2 C(\rho = 0),$$

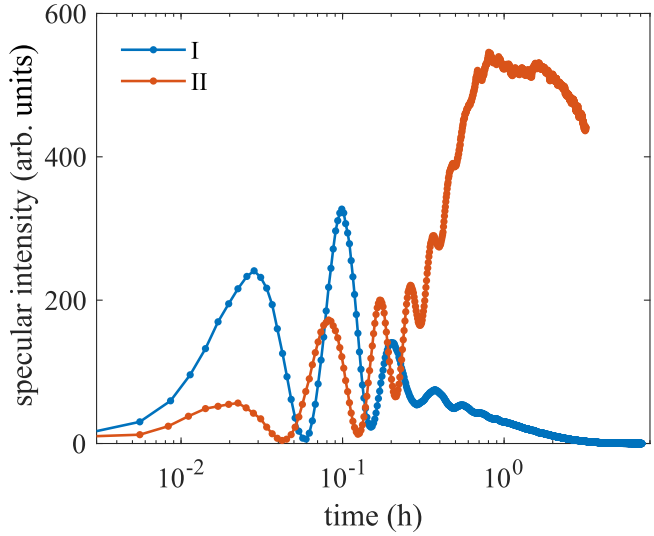

FIG. 9. The specular intensities extracted from the GISAXS patterns; the growth runs I and II.

the projections $S_z(Q_z)$ do not depend on the lateral island shape.

From the GISAXS patterns we also extracted the intensities of the specular peaks; for this extraction we considered the square area depicted in Figs. 8(a)–8(c) by blue rectangles. Figure 9 shows the time dependences of the specular intensities of the growth runs I and II. The intensity oscillations are caused by the interference of the waves reflected from the sapphire/Pt interface, from the wetting-layer/diluted-layer interface, and from the free sample surface.

Figure 10 shows the time evolution of the horizontal $S_\parallel$ [panels (a),(c)] and vertical scans S_z (b),(d) for the growth runs I (a),(b) and II (c),(d), note the logarithmic scale on the horizontal time axes. The $S_\parallel$ scans show side maxima, which have been predicted in the theoretical models in Sec. III. With increasing time, the side maxima get closer and sharper; in the growth run I the distance of the maxima reaches its minimum (nonzero) value at approx. $t = 0.2$h and then remains constant. In run II performed at a higher substrate temperature, the side maxima merge together at $t \approx 0.08$h. These critical times are highlighted by vertical dotted lines in panels (a),(c).

In agreement with theoretical simulations shown above [see Fig. 6, Eq. (6), and the corresponding text], the S_z projections in Figs. 10(b) and 10(d) exhibit side maxima, the distance of which decreases with increasing deposition time. This fact corresponds to the increase of the mean island height h. Unfortunately, the visibility of these maxima gets worse with increasing time, most probably due to an increase of the rms height deviation σ_h, and above approx. $t = 0.3$h the side maxima disappear. There is no distinct time dependence of the Q_z position of the main maximum of S_z, from which the time dependence of the coverage θ could be determined. Most likely, the Pt wetting layer is very thin so that the substrate Yoneda peak is still visible.

Using inverse Hankel transform

$$C(\rho) = \text{const} \int_0^{Q_{\parallel\max}} dQ_\parallel Q_\parallel J_0(\rho Q_\parallel) S_\parallel(Q_\parallel) \qquad (8)$$

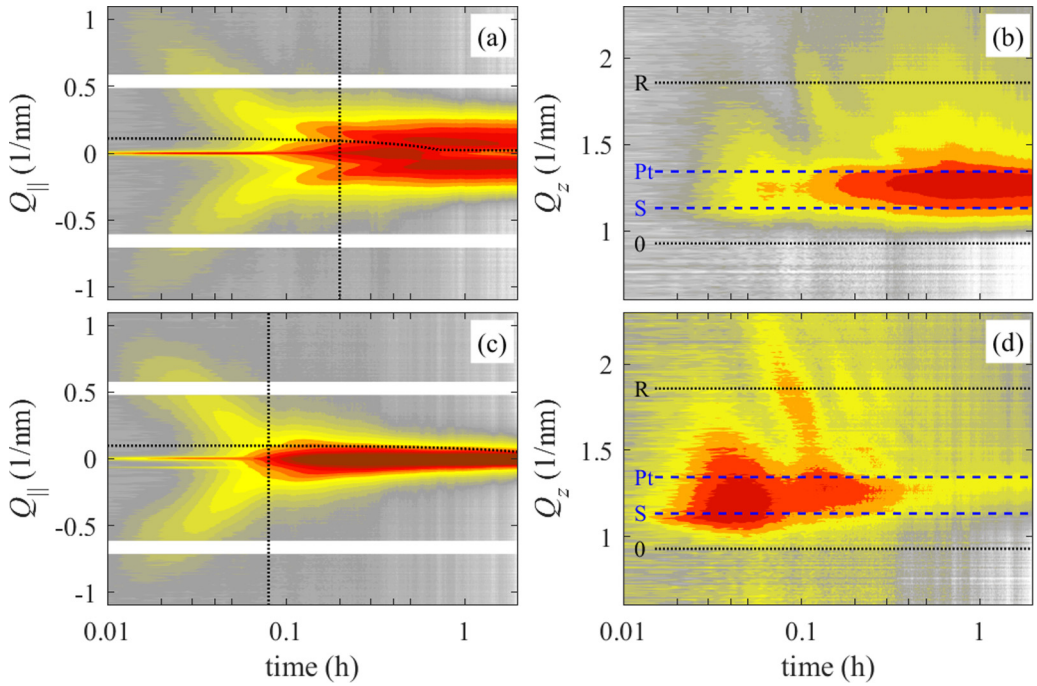

FIG. 10. The time dependence of the extracted $S_\parallel$ (a),(c) and S_z projections (b),(d) in the growth runs I (a),(b) and II (c),(d). The nearly horizontal dotted lines in (a),(c) show the time dependences of $Q_{\parallel\min}$, the vertical dotted lines denote the critical times mentioned in the text. The black dotted lines in (b),(d) represent the positions of the sample horizon (0) and of the reflected peak (R), the blue dashed lines denote the Yoneda wings of sapphire (S) and Pt. The color scale is logarithmic and the colors from white to dark red span over four decades, note the logarithmic scale of the time axis.

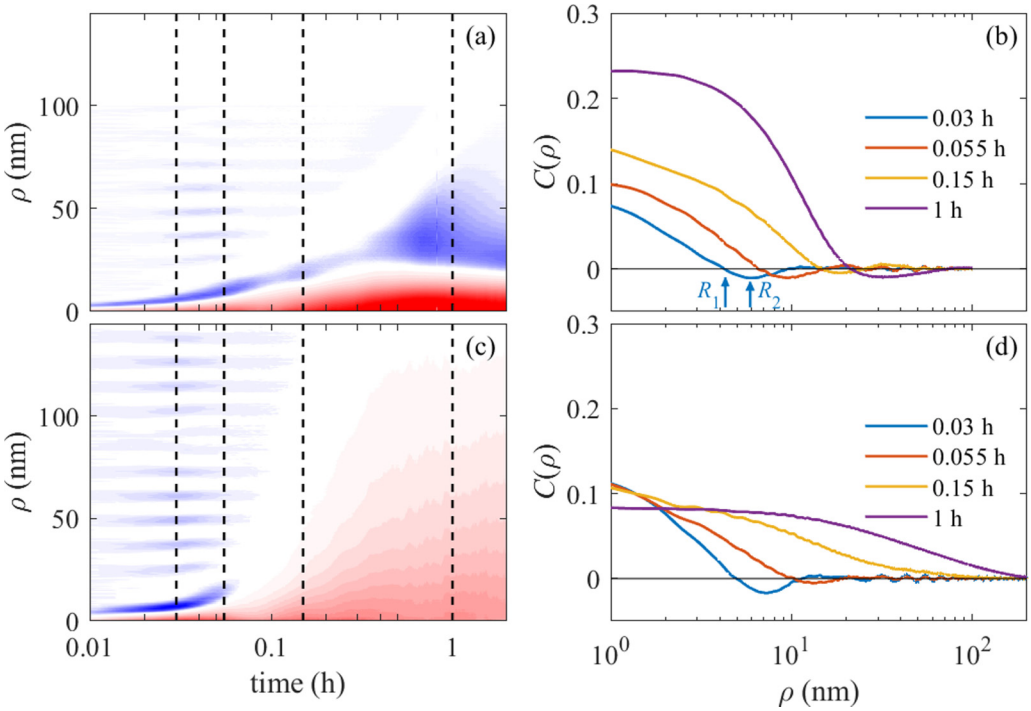

FIG. 11. (a,c) The time dependences of the correlation function $C(\rho)$ calculated from the measured GISAXS data displayed in Fig. 10, the positive (negative) values are displayed by red (blue) colors; for better visibility, the negative interval is ten times exaggerated. The vertical lines denote the time values for which the correlation functions are plotted in panels (b) and (d). The vertical arrows in (b) labeled $R_{1,2}$ denote the characteristic radii for 0.03 h (see text).

we calculated the correlation function $C(\rho)$ from the horizontal scans; the results are plotted in Fig. 11. The upper integration limit in Eq. (8) determines the step size and minimum value of ρ to approx. 5 nm. The maximum value of ρ follows from the sampling theorem $\rho_{\max} = 2\pi/\delta Q_{\parallel} \approx 1\ \mu$m, where $\delta Q_{\parallel}$ is the step size of the experimental dataset. However, this maximum value is not reached in the experimental data, since the correlation function decays to zero already at approx. 100 nm. The multiplicative constant is not important for the analysis of the shape of $C(\rho)$.

In panels (a),(c) the red (blue) areas denote the positive (negative) values of C. The blue-white stripe patterns visible for shortest deposition times in both growth runs are numerical artifacts caused by the numerical integration. The presence of the negative (blue) area for all deposition times in the growth run I [Figs. 11(a) and 11(b)] demonstrates that the islands are still noncoalesced and the PY model can be used for the determination of the lateral island size R and the size of the depleted region R_D for all deposition times. In run II the negative area disappears at approx. $t = 0.1$ h, which is the coalescence threshold. For shorter times, the PY model can be used, after the threshold we can only determine the radii $R_{1,2}$ from $C(\rho)$, as characteristic distances describing the surface morphology.

The analysis of experimental data has been performed in three steps. In the first step, we used the correlation function $C(\rho)$ plotted in Fig. 11 and determined the time dependences of the characteristic radii $R_{1,2}$ defined in Sec. III. In the second step we fitted the horizontal projections $S_{\parallel}(Q_{\parallel})$ to the PY model and determined the time dependence of the mean island radii R, the radii of the depleted zone $R_D = \zeta R$, and the coverages θ. Examples of measured and fitted horizontal projections are shown in Fig. 12; the insets in this figure demonstrate that the asymptotic behavior of horizontal projections agrees with the theoretical prediction shown in Sec. III. The correspondence of the experimental and fitted horizontal projections is very good, however the fitting procedure could be carried out only for horizontal projections with well-developed side maxima, i.e., for run II only at growth times shorter than 0.1 h.

The results of the first two steps are plotted in Fig. 13. The radii R and R_D increase with the growth time t roughly as $t^{0.7}$; the factor $\zeta = R_D/R$ slowly decreases with t and it reaches unity for $t \approx 0.1$ h. The radii R_D are comparable with the characteristic radii R_2. In the growth run II [panels (c) and (d)] the radii $R_{1,2}$ rapidly increase with t for $t > t_{\text{crit}} = 0.06$h; the critical time t_{crit} can be interpreted as the coalescence threshold. At higher time values above approx. 0.15 h the radii $R_{1,2}$ exceed the maximum measurable value of approx. 200 nm; this limit follows from the reciprocal-space resolution of the experimental setup.

The time dependences of the coverage θ are plotted in Figs. 13(b) and 13(d). In the growth run I the surface morphology remains stable during the whole deposition time and the coverage is almost constant $\theta \approx 0.5$; however, the statistical error of θ becomes quite large for longer times. In the growth run II the coverage reaches the value of 0.5 at approx. 0.01 h and then slightly decreases. Above 0.06h the uncertainty of θ is large, as well.

The third step of the data analysis comprises the fitting of the vertical projections $S_z(Q_z)$ to the model in Eq. (1) together with the fitting of the specular intensities plotted in Fig. 9.

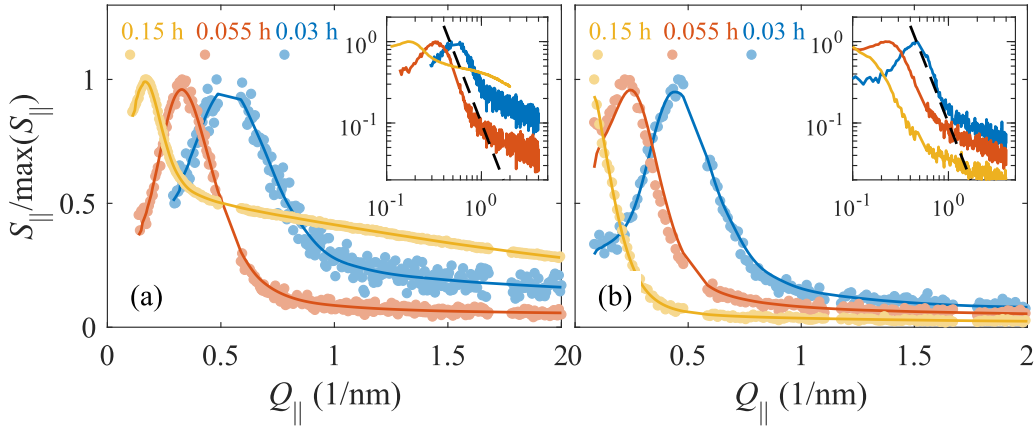

FIG. 12. The horizontal projections $S_\parallel(Q_\parallel)$ extracted from the measured data in Fig. 10, growth runs I (a) and II (b), for three time values (points), and their fits using the PY model (lines). The insets present the measured projections in the loglog scale; the dashed line denotes the slope $Q_\parallel^{-3}$.

For each time value t we performed the S_z- and specular-reflectivity fits in an iterative loop. The specular reflectivity was calculated using the standard Névot-Croce approach [34], considering a (sapphire/Pt wetting layer/effective island layer) sandwich structure. From the S_z fit we determined the mean height h of the islands, its rms deviation σ_h, the thickness $T_{\rm Pt}$ of the wetting layer, and again the coverage θ; these values were used as starting estimates for the specular-reflectivity fit, the result of which is used again in the next S_z-fit step. The coverage affects the vertical projection S_z only indirectly, since it modifies the refraction index of the effective diluted layer containing the islands and consequently slightly affects the amplitudes $A_{\alpha,\beta}$ and the shape of the $S_z(Q_z)$ projection. This is the reason why these coverage values are burdened with large statistical errors. The iterative procedure was applied for the growth times t for which the $S_z(Q_z)$ projections show side maxima; this was the case for $t < 0.6$h and $t < 0.3$ h for the runs I and II, respectively.

Figures 14(a) and 14(c) show examples of the measured and fitted S_z projections; in panels (b) and (d) we plotted the measured and fitted specular intensities. The figures demonstrate that the fitting of the S_z projections was quite successful, however we were not able to achieve a good fit of the specular reflectivity for all time values.

Figure 15 shows the resulting time dependences of the parameters h, $T_{\rm Pt}$, and θ. In the growth run I, both the

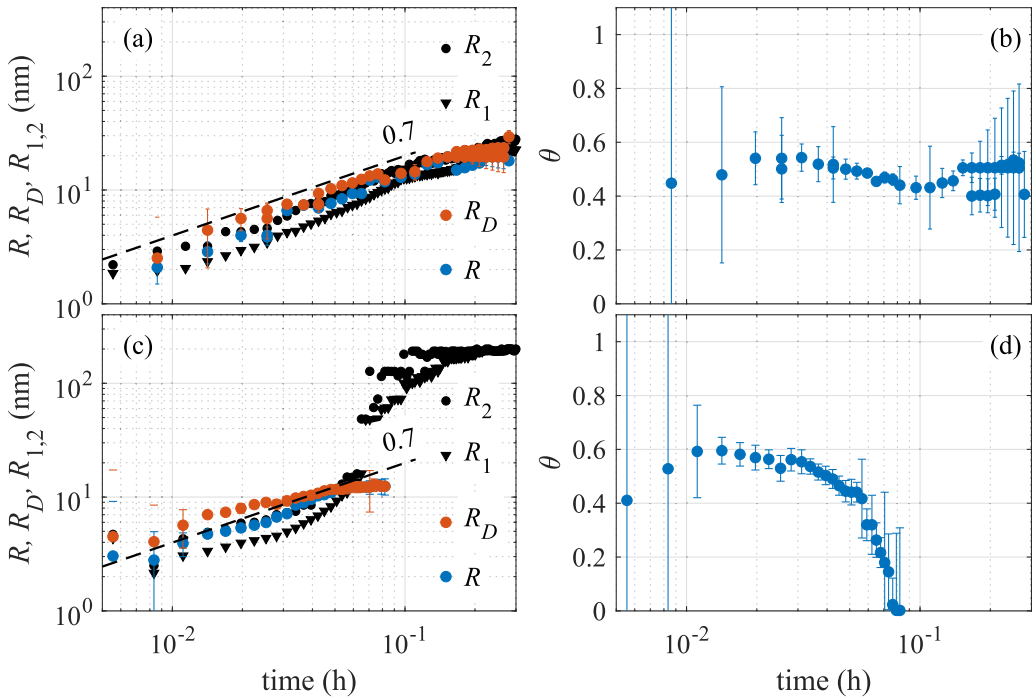

FIG. 13. The evolution of the characteristic radii R, R_D, R_1, and R_2 [panels (a) and (c)] as well as the coverages θ [(b) and (d)] determined from the fit of the measured projections $S_\parallel$ using the PY model. The inclined dashed lines represent the slope of 0.7 (see the text).

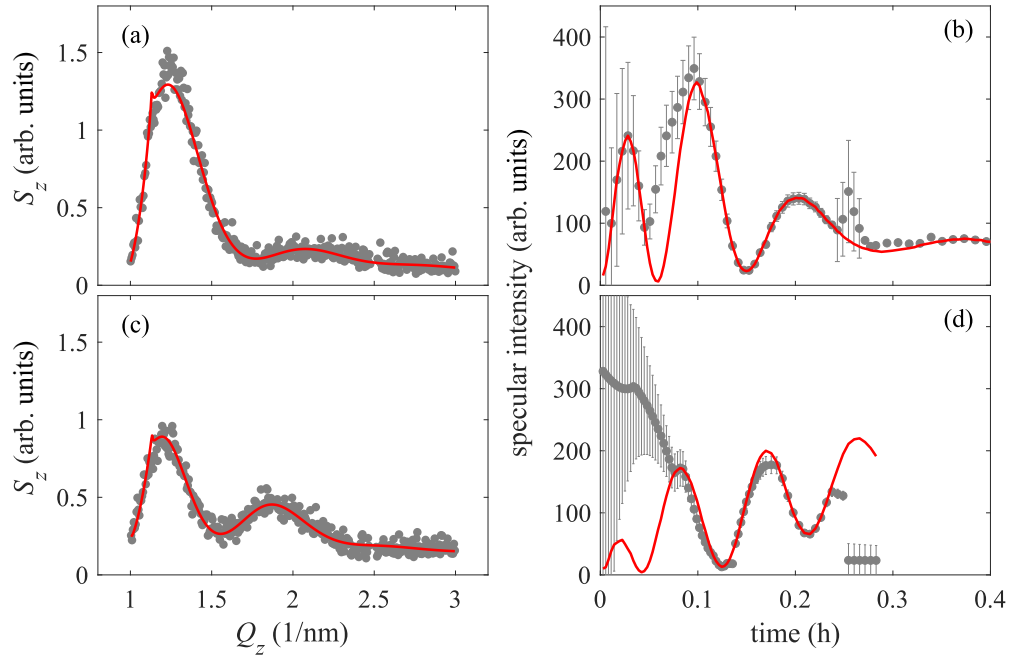

FIG. 14. Examples of the vertical projections S_z (points) and their fits using Eq. (1) (lines); the growth runs I(a) and II(c). In (b),(d) the measured (lines) and fitted (points) specular reflectivities are plotted in the growth runs I (b) and II (d).

island height h and the wetting layer thickness T_{Pt} increase during the deposition. In contrast, the thickness of the wetting layer remains constant during the growth run II and after reaching the threshold time t_{crit} it even decreases and becomes not detectable; the island height steeply increases. The time dependences of the total thickness of the deposited layer $h + T_{\mathrm{Pt}}$ agree well with the expected dependences (black dashed curves) based on growth rates determined from the total Pt thickness measured after the growth completion.

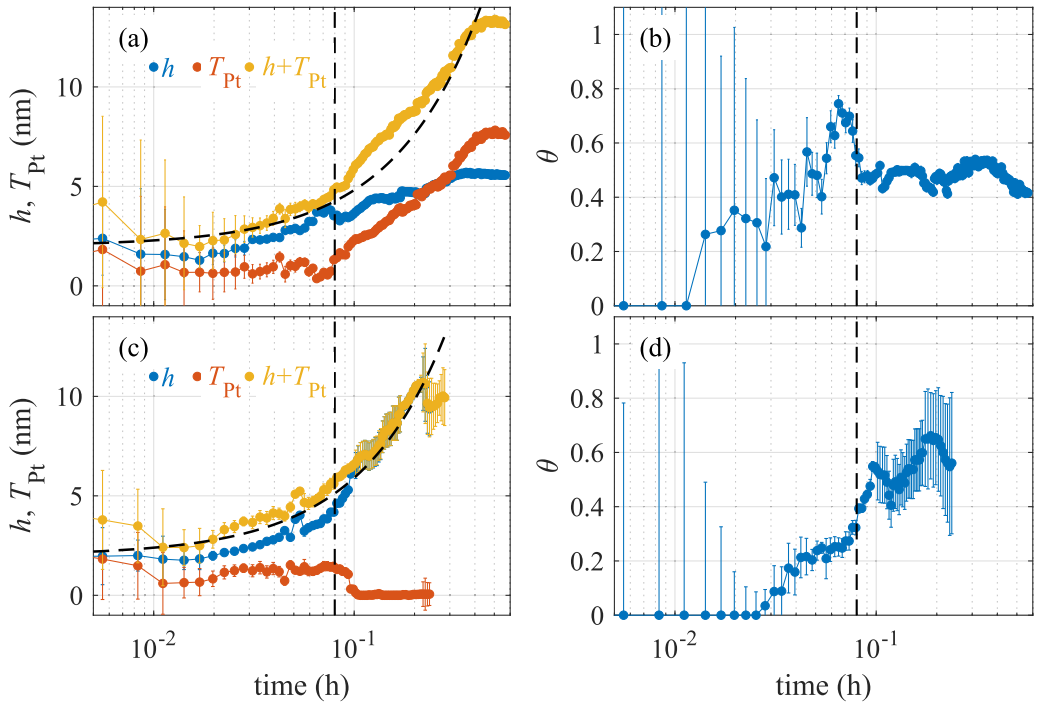

FIG. 15. The time dependences of the parameters h, T_{Pt} determined from the vertical projections; the growth run I (a) and II (c). Panels (b), (d) display the time dependences of the coverage θ. The vertical dashed lines mark the time values for which the vertical projections in Figs. 14(a) and 14(c) are displayed. The black dashed curves in (a) and (c) denote the time evolution of the total Pt thickness deduced from the growth rates determined after the growth completion.

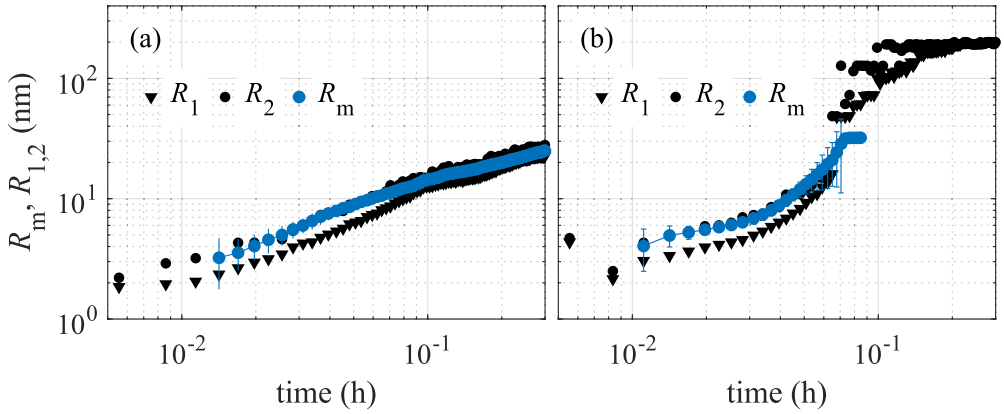

FIG. 16. The characteristic radii $R_{1,2}$ determined from the correlation function $C(\rho)$ compared with the distances R_m from the horizontal projections $S_\parallel$ (see the text). The panels (a) and (b) present the results for the growth runs I and II, respectively.

V. DISCUSSION

In the previous section we described the numerical procedure for determining the characteristic lateral size of the growing surface as well as the mean island height and the thickness of the Pt wetting layer underneath. The numerical calculations are quite demanding, however for the determination of the time evolution of the lateral characteristic distance we can use the value of $R_m = \pi/Q_{\parallel m}$, which can be easily determined form the horizontal projection $S_\parallel(Q_\parallel)$, if it exhibits side maxima. As we showed above, this characteristic radius agrees with the mean island radius with the accuracy of a few tens of percent. Figure 16 compares these values with the characteristic radii $R_{1,2}$ determined from the correlation function $C(\rho)$. It is obvious that R_m well compares with R_2, i.e., with the first minimum of $C(\rho)$. Moreover, Fig. 13 shows that R_2 compares with the mean island radius R determined from the PY model, if applicable. Thus, if a horizontal projection exhibits a side maximum, from its position we easily estimate the island radius $R \approx R_2 \approx R_m = \pi/Q_{\parallel m}$, with the accuracy discussed above. If no side maxima are present, we can determine only $R_{1,2}$ from the correlation function.

The determination of the vertical surface structure (parameters h and T_{Pt}) is more complicated. Equation (6) shows a simple connection between the maxima Q_{zm} of a vertical projection with the mean island height h, however usually only one side maximum is visible in the measured data, so that for a reliable determination of h the knowledge of the coverage θ is necessary. Therefore, without a numerical simulation, the wetting-layer thickness T_{Pt} is not accessible at all. The coverage θ of the surface by the Pt islands was determined both from horizontal $S_\parallel(Q_\parallel)$ and vertical $S_z(Q_z)$ intensity projections, however the reliability of the θ values determined from S_z is much worse. In both growth runs the coverage is approx. 50%, however for longer deposition times t the coverages are burdened by large uncertainties.

Our approach is based on the assumption that the contributions to the diffusely scattered intensity from the lateral and vertical structures can be separated, i.e., the expression for the intensity is assumed as a product of two functions: One depends only on the lateral island size, while the other depends on the island heights and on the wetting layer [see Eq. (1)]. This is the crucial assumption that simplifies substantially the data analysis and makes it possible to determine reliably the time evolution of characteristic lateral and vertical island sizes. Figure 17 demonstrates that this assumption is not always fulfilled; here we present GISAXS patterns taken during the growth run I [(a)–(c)] and II [(d)–(f)], the growth times are indicated in the panels. In panels (b) and (c) the side maxima show oblique streaks (emphasized with dashed black lines) making angles between 70 and 80 deg to the mean sample surface. The streaks can be explained by the presence of facets inclined by 10–20 deg to the surface; most likely, the surface produced in the growth run I is somewhat bumpy. In the growth run II the oblique streaks are not visible, probably the bumpy surface appears as well, however its characteristic lateral distance is larger than the coherence width of the primary x rays and therefore not detectable.

If the lateral and vertical structures cannot be separated, a suitable *a priori* assumption on the island sizes must be made. For instance, one can assume that the islands are self-similar, i.e., the facet angles and the aspect ratios (height vs width) of different islands are equal. This approach leads to a random-fractal model of the island landscape, which lies beyond the scope of this paper. Nevertheless, the island parameters following from the model of separated lateral and vertical structures must be taken with caution, if oblique streaks are detected; in this case they represent mere effective (characteristic) island heights and radii.

For comparison, the surface topography of the two different Pt layers was characterized after growth completion *ex situ* by SE imaging in an SEM. The SE images in Fig. 18 give an overview of the surface peculiarities, whereas those of Fig. 19 reveal more topographic details since they were taken at a fifty thousand times magnification. In more detail, in the case of growth run I [Figs. 18(a) and 18(b)] the Pt surface is relatively rough and the layer is composed of small islands with sizes in the range of approximately 50–100 nm. After growth run II larger aggregates of Pt islands or grains, respectively, are present and the surface seems to be smoothed, which can be explained by the higher deposition temperature of 500 °C. Typical dimensions of these aggregated islands are in the range between few 100 nm and about 2 μm, i.e., they are much larger than the islands found in the Pt layer of growth run I. Furthermore, it should be noted that for

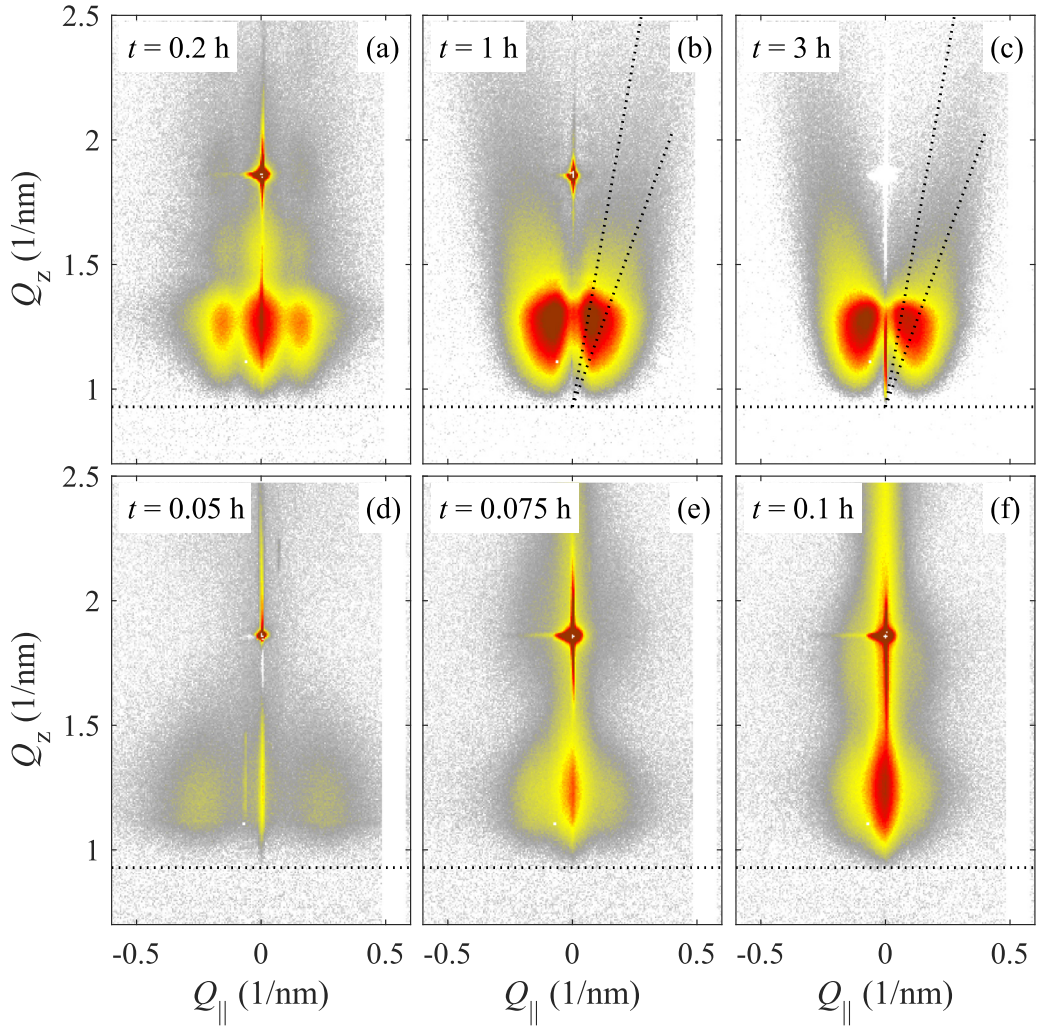

FIG. 17. GISAXS patterns taken during the growth runs I [(a)–(c)] and II [(d)–(f)] at three times t (parameters of the images). The color scale is logarithmic and it spans over three decades. The horizontal dotted lines denote the sample horizon; the oblique lines mark the facet streaks with the angles 70 deg and 80 deg.

the Pt surface after the growth run II the SE images exhibit regions with two clearly different signal intensities, resulting in distinct bright-dark contrast features [cf. Figs. 18(b) and 19(b)]. Presumably, height differences of the two different planar regions in combination with crystal-orientation effects, especially channeling, are the reasons for this contrast phenomenon. With respect to the latter point, it can be assumed that in each type of contrast feature, i.e., brighter or darker

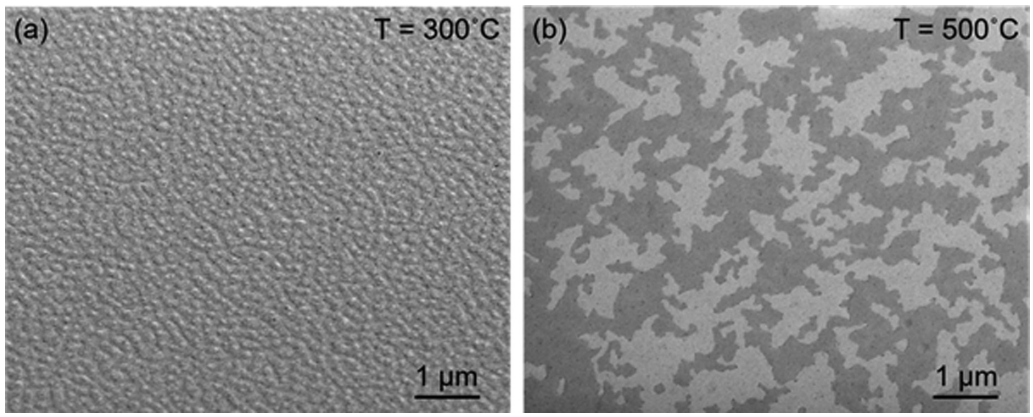

FIG. 18. SEM images of Pt surfaces after the growth run I (a) and II (b).

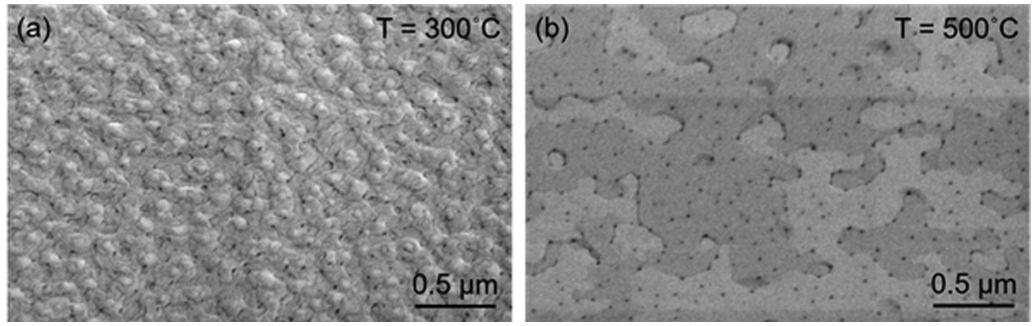

FIG. 19. The SEM images of the same Pt surfaces in a larger magnification; growth runs I (a) and II (b).

region, the Pt grains are grown together with dissimilar in-plane orientation. Besides, in the higher-magnified SE images in Fig. 19(b) dotlike dark contrast features are additionally observable. One possible explanation for their appearance is the presence of threading dislocations, the strain field of which can locally influence the yield of secondary electrons. Because of the use of the through-lens detector at very low primary electron energy (2 keV) even such small surface details are made visible. In general, the results of these SEM investigations support those of the GISAXS measurements, namely that the characteristic lateral sizes of the surface features is approximately 50 nm in the growth run I and several hundreds of nanometer for the run II.

VI. SUMMARY

Using grazing-incidence small-angle x-ray scattering we investigated the development of surface morphology *in situ* during pulsed-laser deposition of Pt on sapphire substrates. The Ornstein-Zernicke theory with the Percus-Yevick model (PY) was used for the analysis of the diffuse scattering profile along the sample surface (lateral direction); this model is applicable if the lateral intensity distribution exhibits distinct satellite maxima, i.e., for isolated surface islands. For coalesced islands we used another approach, consisting of the Monte-Carlo calculation of the island correlation function in real space, and we determined two characteristic surface distances $R_{1,2}$. Comparing the mean island radius R from the PY model with these characteristic distances we found that the distance R_2 in which the correlation function exhibits minimum compares well with R; this radius can be also determined directly from the reciprocal-space position of the satellite maximum.

The vertical sample structure was studied by fitting the vertical distribution of the diffusely scattered intensity to a model based on the distorted-wave Born approximation. Using this method we determined the time evolution of the mean island height as well as the thickness of the Pt wetting layer at the substrate surface.

The analysis method was applied for two growth runs with the substrate temperatures 300 °C (run I) and 500 °C (run II). We found that small isolated islands are present during the whole run I, while island coalescence was observed during run II after approx. 20min of growth. We detected the presence of a thin Pt wetting layer on the substrate surface; in the growth run I both the island height and the wetting layer thickness increase during the deposition, while in run II the wetting layer remains very thin.

ACKNOWLEDGMENTS

The work was supported by the Czech Science Foundation (Project No. 19-10799J) and by the project NanoCent financed by European Regional Development Fund (ERDF, Project No. CZ.02.1.01/0.0/0.0/15.003/0000485). The additional funding by the German Research Foundation within the framework of the Projects No. SCHN 669/11 and No. BA 1642/8-1 is gratefully acknowledged.

[1] G. Renaud, R. Lazzari, and F. Leroy, Surf. Sci. Rep. **64**, 255 (2009).
[2] T. Li, A. J. Senesi, and B. Lee, Chem. Rev. **116**, 11128 (2016).
[3] S. Kowarik, J. Phys.: Condens. Matter **29**, 043003 (2017).
[4] J. R. Levine, J. Cohen, and Y. Chung, Surf. Sci. **248**, 215 (1991).
[5] S. Stemmer, Y. Li, B. Foran, P. S. Lysaght, S. K. Streiffer, P. Fuoss, and S. Seifert, Appl. Phys. Lett. **83**, 3141 (2003).
[6] J. D. Ferguson, G. Arikan, D. S. Dale, A. R. Woll, and J. D. Brock, Phys. Rev. Lett. **103**, 256103 (2009).
[7] J. D. Brock, J. Ferguson, Y. Kim, H. Q. Wan, and A. R. Woll, Mater. Sci. Eng. A **528**, 72 (2010).
[8] L. C. Arslan, C. Sanborn, E. Anzenberg, and K. F. Ludwig, Jr., Phys. Rev. Lett. **109**, 106102 (2012).
[9] M. Schwartzkopf, A. Buffet, V. Korstgens, E. Metwalli, K. Schlage, G. Benecke, J. Perlich, M. Rawolle, A. Rothkirch, B. Heidmann, G. Herzog, P. Mueller-Buschbaum, R. Roehlsberger, R. Gehrke, N. Stribeck, and S. V. Roth, Nanoscale **5**, 5053 (2013).
[10] M. Schwartzkopf, G. Santoro, C. J. Brett, A. Rothkirch, O. Polonskyi, A. Hinz, E. Metwalli, Y. Yao, T. Strunskus, F. Faupel, P. Mueller-Buschbaum, and S. V. Roth, ACS Appl. Mater. Interfaces **7**, 13547 (2015).
[11] G. Eres, J. Z. Tischler, C. M. Rouleau, H. N. Lee, H. M. Christen, P. Zschack, and B. C. Larson, Phys. Rev. Lett. **117**, 206102 (2016).

[12] C. Revenant, G. Renaud, R. Lazzari, and J. Jupille, Nucl. Inst. Methods Phys. Res. B **246**, 112 (2006).
[13] G. Kaune, M. A. Ruderer, E. Metwalli, W. Wang, S. Couet, K. Schlage, R. Rohlsberger, S. V. Roth, and P. Muller-Buschbaum, ACS Appl. Mater. Interfaces **1**, 353 (2009).
[14] G. Santoro, S. Yu, M. Schwartzkopf, P. Zhang, S. K. Vayalil, J. F. H. Risch, M. A. Rübhausen, M. Hernández, C. Domingo, and S. V. Roth, Appl. Phys. Lett. **104**, 243107 (2014).
[15] S. Yu, G. Santoro, Y. Yao, D. Babonneau, M. Schwartzkopf, P. Zhang, S. K. Vayalil, P. Wessels, R. Dohrmann, M. Drescher, P. Muller-Buschbaum, and S. V. Roth, J. Phys. Chem. C **119**, 4406 (2015).
[16] M. Schwartzkopf and S. V. Roth, Nanomaterials **6**, 239 (2016).
[17] M. Hodas, P. Siffalovic, M. Jergel, M. Pelletta, Y. Halahovets, K. Vegso, M. Kotlar, and E. Majkova, Phys. Rev. B **95**, 035424 (2017).
[18] R. Hosemann and S. N. Bagchi, *Direct Analysis of Diffraction by Matter* (North-Holland, Amsterdam, 1962).
[19] J. L. Eads and R. P. Millane, Acta Cryst. A **57**, 507 (2001).
[20] R. Lazzari, J. Appl. Crystallogr. **35**, 406 (2002).
[21] D. Babonneau, J. Appl. Crystallogr. **43**, 929 (2010).
[22] L. S. Ornstein and F. Zernicke, Proc. Acad. Sci. Amsterdam **17**, 793 (1914).
[23] J. K. Percus and G. J. Yevick, Phys. Rev. **110**, 1 (1958).
[24] P. Jensen, Rev. Mod. Phys. **71**, 1695 (1999).
[25] C. Ratsch and J. A. Venables, J. Vac. Sci. Technol. A **21**, S96 (2003).
[26] J. W. Evans, P. A. Thiel, and M. C. Bartelt, Surf. Sci. Rep. **61**, 1 (2006).
[27] A. Chatterjee and D. G. Vlachos, J. Comput.-Aided Mater. Des. **14**, 253 (2007).
[28] S. K. Sinha, E. B. Sirota, S. Garoff, and H. B. Stanley, Phys. Rev. B **38**, 2297 (1988).
[29] S. Bauer, S. Lazarev, A. Molinari, A. Breitenstein, P. Leufke, R. Kruk, H. Hahn, and T. Baumbach, J. Synchr. Radiat. **21**, 386 (2014).
[30] S. Bauer, A. Rodrigues, L. Horák, X. Jin, R. Schneider, T. Baumbach, and V. Holý, Materials **13**, 61 (2020).
[31] M. Rauscher, T. Salditt, and H. Spohn, Phys. Rev. B **52**, 16855 (1995).
[32] P.-z. Wong and A. J. Bray, Phys. Rev. Lett. **60**, 1344 (1988).
[33] X. Guo and U. Riebel, J. Chem. Phys. **125**, 144504 (2006).
[34] L. Névot and P. Croce, Phys. Rev. Appl. (Paris) **15**, 761 (1980).